ARTICLE

Effect of Structure and Size on the Electrical Properties of Nanocrystalline WO_3 Films

R.S. Vemuri, K. Kamala Bharathi, S.K. Gullapalli, and C.V. Ramana*

Department of Mechanical Engineering, University of Texas at El Paso, El Paso, Texas 79968

ABSTRACT Nanocrystalline WO_3 films were grown by reactive magnetron sputter-deposition by varying the substrate temperature in the range of 303(RT)−673 K. The structure and electrical transport properties of WO_3 films were evaluated using X-ray diffraction and dc electrical conductivity measurements. The effect of ultramicrostructure and grain-size was significant on the electrical properties of WO_3 films. DC conductivity variation of the WO_3 films measured in the temperature range of 120−300 K reveals their semiconducting nature. The temperature dependent electrical conductivity curves exhibit two distinct regions indicative of two different types of electrical transport mechanisms. Analysis of the conductivity indicates that the small polaron and variable-range-hopping mechanisms are operative in 180−300 K and 120−180 K temperature regions, respectively. The density of localized states at the Fermi level, $N(E_F)$, has been calculated and it was found to be $\sim 1 \times 10^{19}$ eV^{-1} cm^{-3} for all the films.

KEYWORDS: WO_3 thin films • H_2S sensors • size effects • electrical properties • small polaron hopping • variable range hopping

I. INTRODUCTION

Semiconducting oxides received significant recent attention as sensor materials because of their remarkable electrical properties sensitive to oxidative or reductive type of gases (1–4). Currently, there has been a great deal of interest in WO_3 low-dimensional structures for a wide variety of applications in chemical and mechanical sensors, selective catalysis, electrochemical industry and environmental engineering (5–9). It has been demonstrated that the sensing properties of WO_3 films will have numerous applications in environmental and industrial pollution monitoring (5–9). WO_3 films exhibit excellent functional activity to various gases, such as H_2S, NO_x, trimethylamine, and other organics, and are suitable for integrated sensors (5–9). Most importantly, WO_3 nanocrystalline films have been established as one of the best gas sensors for the reducing gases such as NO_2, H_2, and CO and the results evidenced the role of the microstructure, specifically the grain size (5–9). Because of the large surface to volume ratio and smaller dimensions, WO_3 nanostructures appear to be promising candidates for chemical sensors working at various temperatures, which include low and high temperatures (10). In addition, WO_3 is an intensively studied representative of a group of "chromogenic" materials because of the coloration effects associated with various processes (11–14). WO_3 has been in use for the development of smart windows for energy-efficient architecture of buildings and automobiles, flat-panel displays, optical memory and writing-reading-erasing devices, and electronic information displays. Most of these applications depend on the remarkable electrical and optical properties of WO_3 (15). Therefore, the controlled growth, fundamental understanding, and manipulation of electronic properties of WO_3 at the nanoscale dimensions has important implications for the sensor design and utilizing WO_3 films.

The electrical properties, and hence the sensor performance of WO_3 films, is dependent on the microstructure, which in turn depends on the technique used to fabricate the films and the growth conditions. The microstructure factors such as grain size (L), grain boundary, film thickness, specific phase, dopants (if any), and active surface offered for reaction with the test gases will, therefore, play a significant role in determining the ultimate sensing performance of WO_3 nanostructures. However, WO_3 is a complicated material with respect to crystal structure and thermal stability because of several structures, such as monoclinic, triclinic, tetragonal, orthorhombic, cubic, and hexagonal, for pure and oxygen deficient WO_3 (16–18). At room temperature, WO_3 crystallizes in a triclinic structure and exhibit structural transformation at higher temperatures (16–19). Investigations on bulk WO_3 report the following sequence: triclinic (~17 °C) → monoclinic (330 °C) → orthorhombic (740 °C) → tetragonal. In addition to that, formation of pyrochlore WO_3 structure at about 373 K has been reported (20). Furthermore, WO_3 films prepared by various techniques (20–23) and under various processing conditions usually possess different microstructures and properties. Therefore, the control of microstructure and the fundamental understanding of the effect of microstructure on the electrical properties of WO_3 need a significant attention for both theoretical (24, 25) and experimental investigations. Clearly, controlled growth and manipulation of specific crystal structures at the nanoscale dimensions has important implications for the design and applications of WO_3-based sensors. The ability to tailor the properties so as to optimize sensor performance requires a detailed fundamental understanding of the relationship between the microstructure and

* Corresponding author. E-mail: rvchintalapalle@utep.edu.
Received for review May 21, 2010 and accepted August 1, 2010
DOI: 10.1021/am1004514
2010 American Chemical Society

ARTICLE

electrical properties of WO_3, particularly at the nanoscale dimensions.

In the present work, the microstructure and temperature-dependence of electrical conductivity of nanocrystalline WO_3 films made by radio frequency magnetron sputtering are investigated. WO_3 films were produced at various substrate temperatures ranging from room-temperature (RT/303 K) to 673 K. The purpose is not only to obtain films with a variable microstructure and nanometrics but also to cover the range of temperatures that are usually required either for postannealing or film processing of WO_3 for sensors as reported in the literature. To explain electrical transport properties, we have considered several conduction mechanisms as relevant to oxide semiconductors. These models include the simple thermally activated conduction, grain-boundary conduction, small-polaron hopping conduction, and variable-range hopping (VRH) conduction. An analysis of the conduction mechanisms at various temperature ranges and a correlation between microstructure and electrical properties in nanocrystalline (nc-WO_3) W—O films is presented and discussed in detail in this paper.

2. EXPERIMENTAL SECTION

WO_3 thin films were deposited onto silicon (Si) wafers by radio frequency (RF) (13.56 MHz) magnetron sputtering. The Si(100) substrates were cleaned by RCA (Radio Corporation of America) cleaning. All the substrates were thoroughly cleaned and dried with nitrogen before introducing them into the vacuum chamber, which was initially evacuated to a base pressure of $\sim 1 \times 10^{-6}$ Torr. Tungsten (W) metal target (Plasmaterials Inc.) of 3″ diameter and 99.95% purity was employed for reactive sputtering. The W-target was placed on a 3-in. sputter gun, which is placed at a distance of 8 cm from the substrate. A sputtering power of 40 W was initially applied to the target while introducing high purity argon (Ar) into the chamber to ignite the plasma. Once the plasma was ignited the power was increased to 100 W and oxygen (O_2) was released into the chamber for reactive deposition. The flow of the Ar and O_2 and their ratio was controlled using as MKS mass flow meters. Before each deposition, the W-target was presputtered for 10 min using Ar alone with shutter above the gun closed. The samples were deposited at different temperatures (T_s) varying from RT-673 K. The substrates were heated by halogen lamps and the desired temperature was controlled by Athena X25 controller.

The grown WO_3 films were characterized by performing structural and electrical measurements. X-ray diffraction (XRD) measurements on WO_3 films were by performed using a Bruker D8 Advance X-ray diffractometer. All the measurements were made ex-situ as a function of growth temperature. XRD patterns were recorded using Cu Kα radiation ($\lambda = 1.54056$ Å) at RT. The coherently diffracting domain size (d_{hkl}) was calculated from the integral width of the diffraction lines using the well-known Scherrer's equation (26) after background subtraction and correction for instrumental broadening. Surface imaging analysis was performed using a high-performance and ultra high resolution scanning electron microscope (Hitachi S-4800). The secondary electron imaging was performed on WO_3 films grown on Si wafers using carbon paste at the ends to avoid charging problems. The grain detection, size-analysis and statistical analysis was performed using the software provided with the SEM. The average grain size measured was found to vary from 9 to 50 nm as reported elsewhere (27). DC electrical resistivity measurements were carried out under the vacuum of 10^{-2} Torr by two-probe method in the temperature range 120—300 K employing a closed cycle refrigerator (CCR). Resistance was measured by employing a Keithley electrometer (Keithley 6517A Electrometer/High resistance meter). The temperature was measured using a silicon diode sensor and employing a Lakeshore temperature controller (model 330). The film was kept on the cold head of the CCR. The point contacts were made by soldering the indium metal at the corners of the films.

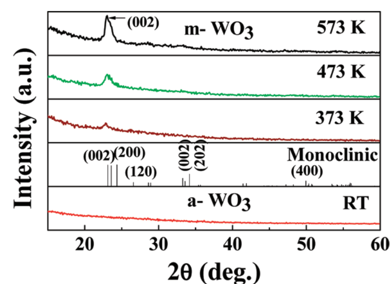

FIGURE 1. XRD patterns of WO_3 films grown at $T_s \leq 573$ K. It is evident from the curves that the films grown at RT are amorphous whereas films grown at $T_s \geq 373$ K are nanocrystalline. Films crystallize in m-WO_3 phase. XRD pattern of m-WO_3 (PDF: 830950) is also included for reference. WO_3 films grown at 573 exhibit a mixture of monoclinic and tetragonal phases.

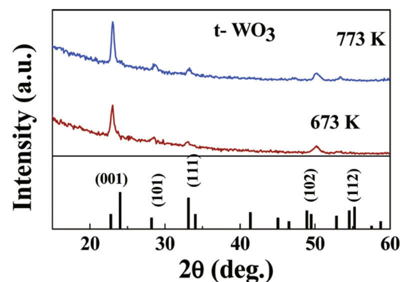

FIGURE 2. XRD patterns of WO_3 films grown at $T_s \geq 673$ K. The curves indicate that WO_3 films crystallize in tetragonal structure. XRD pattern of t-WO_3 (PDF:also included for comparison.

3. RESULTS AND DISCUSSION

The XRD patterns of WO_3 films are shown in Figures 1 and 2 as a function of T_s. The XRD curve (Figure 1) of WO_3 films grown at RT did not show any peaks indicating their amorphous (a-WO_3) nature. The XRD peak corresponding to monoclinic WO_3 (m-WO_3) phase appears when the $T_s = 373$ K. However, the peak (at 23.1°) is rather broad, indicating the presence of very small nanoparticles. It is evident (Figure 1) that the intensity of the peak, at 23.1°, which corresponds to diffraction from (002) planes increase with increasing T_s (28). This is an indicative of an increase in the average crystallite-size and preferred orientation of the film along (002) with increasing T_s. The later is dominant for WO_3 films grown at $T_s \geq 473$ K. Also, a structural transformation occurs at $T_s = 673$K. XRD peaks due to tetragonal (t-WO_3) phase are clearly seen for WO_3 films grown at $T_s \geq 673$ K (Figure 2). In fact, it can be seen in the XRD curve obtained for WO_3 films grown at 573 K that an overlap of (001) peak corresponding to t-WO_3 and (002) peak corresponding to m-WO_3 indicating the onset of phase transformation but not complete. Perhaps, the temperature is just sufficient to induce a phase change in nanoscale m-WO_3 films but not fully favorable to complete the process. High-temperature

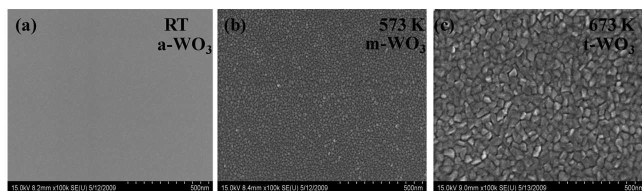

FIGURE 3. SEM images of WO_3 films grown at various temperatures. The phases determined from XRD are as indicated.

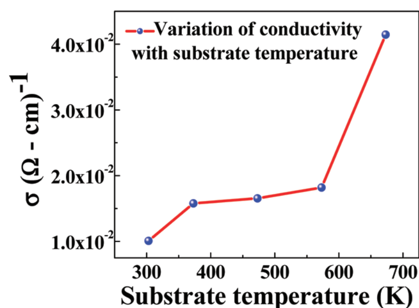

FIGURE 4. Room-temperature conductivity value for WO_3 films grown at different substrate temperatures.

t-WO_3 formation at 673 K seems to be the effect of phase stabilization at the nanoscale dimensions. The preferred *c*-axis orientation could be due to the growth process minimizing the internal strain-energy in the film. Anisotropy exists in crystalline materials and the strain energy densities will typically be different for different crystallographic direction. The growth will favor those orientations with low strain energy density. Therefore, increasing T_s favors the preferred orientation along (002) while minimizing the strain-energy in the WO_3 film. The SEM images of WO_3 films as a function of substrate temperature are shown in Figure 3. The effect of temperature on the surface morphology of WO_3 films is remarkable. No features can be seen for WO_3 films grown at RT even at very high magnifications (Figure 3a). This observation is in agreement with the XRD results indicating the complete amorphous nature of the samples. The small, dense particles spherical in shape can be noticed in SEM image (Figure 3b) for WO_3 films grown at 473 K. The SEM data along with appearance of diffraction peaks in XRD clearly indicate that 473 K is the critical temperature to promote the growth of nanocrystalline WO_3 films. The XRD and SEM results suggest that a further increase in temperature beyond 473 K results in changes in the crystal structure and morphology. WO_3 films continue to show preferred growth along with an increase in average particle size with increasing temperature. It can be seen in SEM image (Figure 3c) that increasing temperature to 573 K results in size >20 nm.

The room-temperature electrical conductivity variation of WO_3 films with T_s is shown in Figure 4. It can be seen that the electrical conductivity increases with increasing T_s. The conductivity is reported to decrease with grain size reduction due to the increasing grain boundary volume and associated impedance to the flow of charge carriers (29, 30). If the crystallite size is smaller than the electron mean free path, grain boundary scattering dominates and hence the electrical conductivity decreases. The electrical resistivity is also

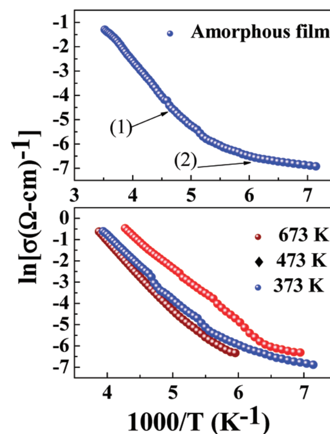

FIGURE 5. Temperature-dependent dc conductivity of WO_3 films.

very sensitive to lattice imperfections in solids, such as vacancies and dislocations that are reported to be present in nanocrystalline materials. In addition to that, lattice strain and the distortions can affect the motion of charge causing decrease in conductivity (29–31). The room-temperature conductivity data and its variation with T_s observed for WO_3 can be explained taking these factors into consideration. WO_3 films grown at RT are completely amorphous as evidenced in XRD studies. The randomness or disordered structure of the films, therefore, accounts for the observed low conductivity of a-WO_3 films. Appearance of diffraction peaks in the XRD curves, an increase in the average crystallite size along with a preferred orientation of the film along (002) is clearly seen with increasing T_s. Therefore, increase in conductivity with increasing T_s can be attributed to the increasing crystalline nature and preferred orientation of the film along (002). In addition, a decrease in strain energy of the growing WO_3 film, as discussed using the XRD results, with increasing T_s also causes the increase in conductivity. The observed jump in the electrical conductivity for WO_3 films grown at 673 K seems to be a result of combined effect of the grain-size increase and phase transformation from m-WO_3 to t-WO_3. The observed variation in electrical conductivity is in correlation with optical properties, where we found enhancement in the band gap for a-WO_3 films and continuous decrease in the band gap with increasing temperature or grain size (32).

The temperature-dependent electrical conductivity plots of WO_3 films are shown in Figure 5. Conductivity decreases exponentially with decreasing temperature from 300 to 120 K which indicates the semiconducting nature of all the WO_3 films. However, a marked difference in the temperature-dependence of conductivity can be seen for a-WO_3 films (Figure 5a) when compared to nc-WO_3 films (Figure 5b). Similarly, in Figure 4b, it can be seen that the curves of WO_3 films grown at 373 and 473 K are clearly separated from WO_3 films grown at 673 K. We attribute this behavior to the grain-size and phase transformation. The size variation for the films grown between 373 and 473 K is small but significantly lower when compared films grown at 673 K (24, 32). Also, phase transformation occurs from m-WO_3 to t-WO_3 at 673 K. The most remarkable feature of these

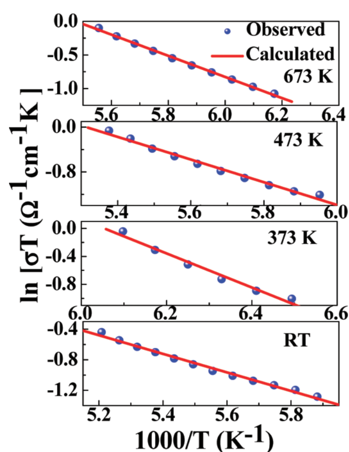

FIGURE 6. Relation between ln σT and 1000/T for WO_3 thin films.

temperature-dependent electrical conductivity curves of WO_3 films is two distinct regions indicative of two different conduction mechanisms operative in those temperature regions.

The temperature-dependence of conductivity of a-WO_3 film (Figure 5a) shows almost a linear behavior at high temperatures ($T > 250$ K) and a curvature at low temperatures. It can also be noticed that the activation energy continuously decreases with a decrease in measuring temperature of the conductivity. The curvature without a definite slope and continuous decrease in activation energy is a characteristic behavior of polaron hopping mechanism in amorphous semiconductors. On the other hand, the conductivity plots show a distinct change in slope at a more or less same temperature in nc-WO_3 films (Figure 4b). We consider various models to analyze the observed electrical properties and conduction mechanisms as discussed below.

Conductivity in semiconductors is due to both hopping of electrons and charge transport via excited states and it can be expressed as (33, 34)

$$\sigma = A_1\exp\left(\frac{-E_1}{k_BT}\right) + A_2\exp\left(\frac{-E_2}{k_BT}\right) + A_3\exp\left(\frac{-E_3}{k_BT}\right) + \tag{1}$$

where E_1 is the activation energy for intrinsic conduction and E_2, E_3, ..., are the activation energies needed for hopping conduction. A_1, A_2, A_3 are constants and k_B is the Boltzmann constant. Ln σ vs 1000/T plots (Figure 6) yield two different slopes for WO_3 films. The activation energy values at different temperature ranges (300−180 K and 180−120 K) calculated from the ln σ vs 1000/T plots are given in Table 1. The activation energy is found to be higher in the 300−180 K temperature region when compared that in the 180−120 K temperature region. Decreasing activation energy with decreasing temperature in transition metal oxides has been explained by small-polaron theory (34). The VRH model of small polarons also predicts continuously decreasing activation energy with decreasing temperature. Small polaron formation occurs for strong enough electron−phonon interaction, as predicted by Landau (35). The polaron transport occurs by hopping process at sufficiently higher temperatures. The multiphonon hopping process freezes out at lower temperatures, and conduction through extended states in a polaron band dominates. This should lead to a decay of the conductivity and activation energy as the temperature is reduced well below half of the Debye temperature (36).

To obtain a clear distinction between the two conduction mechanisms (two different slopes in Figure 5), we used the polaron and variable-range hopping (VRH) models to fit the conductivity data of WO_3 films. In the temperature regime, 180−300 K, the conductivity data of WO_3 films can be interpreted in terms of the phonon-assisted hopping model given by Mott (37)

$$\sigma = \frac{e^2\nu_{ph}c(1-c)}{k_BTR}\exp(-2\alpha R)\exp\left(-\frac{E}{kT}\right) \tag{2}$$

where ν_{ph} is the optical phonon frequency, c is the fraction of reduced transition metal ions (the ratio of ion concentration of transition metal ions in the low valence state to the total concentration of transition metal ions), R is the average spacing between the transition ions, α is the localization length, and E is the activation energy for the hopping conduction. The plots of ln σT vs 1000/T for WO_3 films are shown in Figure 6. The values of ν_{ph} and R, the activation energy, E (calculated from the slope of the plot) are given in Table 1. Assuming a strong electron−phonon interaction, Austin and Mott proposed that

$$E = E_H + \frac{E_D}{2} \tag{3}$$

for ($T > \theta_D/2$)

$$E = E_D \tag{4}$$

for ($T > \theta_D/4$) where E_H is the polaron hopping energy, E_D is the disorder energy arising from the energy difference of neighbors between two hopping sites and θ_D is the Debye temperature (380 K for WO_3). Polaron radius can be calculated using the formula (35–37)

$$r_p = \left(\frac{\pi}{6}\right)^{1/3}\left(\frac{R}{2}\right) \tag{3a}$$

Where R is the average distance between the transition metal ions (W ion), which is 0.3 nm in the present case (38). The value of r_p was found to be 0.12 nm.

To better understand the nature of hopping conduction, i.e., to determine whether it is adiabatic or nonadiabatic regime, it is necessary to perform a detailed analysis. The following are the conditions that define the adiabatic and nonadiabatic conduction

Table 1. Activation Energy Values, A and B Parameter Values, and the Density of Localized States at the Fermi Level Values of WO_3 Thin Films

substrate temperature of WO_3 film (°C)	activation energy (eV) 180−300 K	activation energy (eV) 120−180 K	A (Ω^{-1} cm^{-1} K$^{1/2}$)	B (K$^{1/4}$)	$N(E_F)$ (× 10^{19} eV^{-1} cm^{-3})
RT	0.22	0.029	73242	23.27	2.72
100	0.23	0.031	73602	23.89	2.71
200	0.25	0.033	72266	23.83	2.67
400	0.26	0.033	72572	23.48	2.65

$$J > \left(\frac{2kTE_H}{\pi}\right)^{1/4}\left(\frac{h\nu_0}{\pi}\right)^{1/2} \quad \text{(adiabatic)} \tag{4a}$$

$$J < \left(\frac{2kTE_H}{\pi}\right)^{1/4}\left(\frac{h\nu_0}{\pi}\right)^{1/2} \quad \text{(nonadiabatic)} \tag{5}$$

where J is the polaron bandwidth, E_H is the hopping energy (0.22 eV), and $h\nu_0 = k_B\theta_D$ (θ_D is the Debye temperature and it is 380 K for WO_3). In the evaluation of the term on the right-hand side of eq 5 at 300 K, a value of 0.0222 eV is obtained. On the other hand, J can be estimated independently using Dhawan's formula (36)

$$J \approx e^3\left(\frac{N(E_F)}{(\varepsilon_p)^3}\right)^{1/2} \tag{6}$$

Where ε_p is the effective dielectric constant and it can be calculated using the Mott's small polaron hopping model with the relation by

$$E_H = \left(\frac{e^2}{4\varepsilon_p}\right)\left(\frac{1}{r_p} - \frac{1}{R}\right) \tag{7}$$

In the present case, the value of ε_p was found to be 7.4. By using the previously obtained $N(E_F)$ and ε_p values, J is calculated as 0.0028 eV. Because $J < 0.0222$ eV, we conclude that the electrical transport in WO_3 is due to small-polaron conduction in the nonadiabatic regime.

According to the small-polaron theory and the VHR model of small polarons, the activation energy should continuously decrease with decreasing temperature. The procedure suggested by Greaves as a modification of Mott's model of VRH could be applied in the second temperature regime (120−180 K), and the following expression is proposed for the electrical conductivity

$$\sigma T^{1/2} = A\exp(-BT^{-1/4}) \tag{8}$$

Where A and B are constants and B is expressed as

$$B = 2.1\left[\frac{\alpha^3}{k_B N(E_F)}\right]^{1/4} \tag{9}$$

$N(E_F)$ is the density of localized states at E_F and α^{-1} is the decay constant of the wave function of localized states at E_F.

Variable-range hopping model may be valid in the temperature range 120−180 K and a good fit of the experimental data to the eq 9 is shown in Figure 7 ($\ln(\sigma T^{1/2})$ vs $T^{-1/4}$ plot). The values of parameters A and B were calculated from this curve and are shown in Table 1. The density of localized states at the Fermi level, $N(E_F)$, has been calculated taking a constant value of α^{-1} (× 10^{-7} cm) (38). The determined value is $N(E_F) \approx 1 \times 10^{19}$ eV^{-1} cm^{-3}, which is good agreement with the reported value for WO_3 films (39, 40). Electrical properties of WO_3 thin films prepared by thermal evaporation have been reported by M G Hutchins et al. (40). Arrhenius law, a polaron model, and a variable-range hopping model have been used to explain the conduction mechanism forWO_3 films at different temperature regime. Using the variable-range hopping model, the density of localized states at the Fermi level, $N(E_F)$, was reported to be to be 1.08×10^{19} eV^{-1} cm^{-3}. The average values of activation energies were found to be 1.70 eV ($T > 525$ K), 0.58 eV (525 K ≤ T ≤ 353 K,) and 0.06 eV ($T \leq 353$ K).

A good fit of the Mott's VRH model has been verified by calculating the hopping parameters and the Mott's requirements (24) ($R_{hop}\alpha \geq 1$ and $E_{hop} > k_BT$). Here, R_{hop} and E_{hop} are temperature-dependent hopping distance and average polaron hopping energy, respectively.

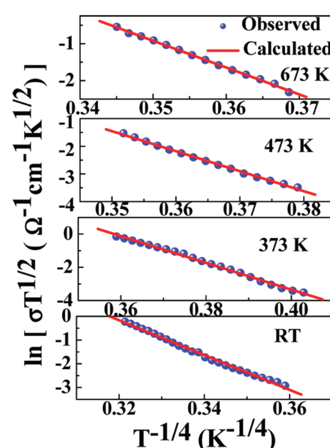

FIGURE 7. Relation between ($\ln(\sigma T^{1/2})$ and $T^{-1/4}$ for WO_3 thin films.

ARTICLE

$$R_{hop} = \left[\frac{9}{8\pi N(E_F)\alpha k_B T}\right]^{1/4} \quad (10)$$

$$E_{hop} = \frac{3}{4\pi R_{hop}^3 N(E_F)} \quad (11)$$

The calculated average values of R_{hop} and E_{hop} at 140 K for WO_3 films are found to be 3.9 nm and 204 meV. The values of $R_{hop}\alpha$ and E_{hop} are found to be 3.9 and 204 meV, respectively. The requirements ($R_{hop}\alpha \geq 1$ and $E_{hop} > k_BT$) are clearly satisfied.

The effect of microstructure and size on the electrical properties of WO_3 films as determined in this work is quite useful while considering the fundamental aspects and design of a sensor. The key dimension defining the enhancement of a sensor performance as function of reducing particle size or film thickness is the Debye length (λ_D) (41, 42). Most important to mention is that the grain size must be very small on the order of λ_D, where the space-charge regions overlap and all the grains are fully depleted, to take the advantage of nanoscale effects. It has been reported that the better sensor performance was obtained for nanocrystalline SnO_2 films with very small sizes ($\leq\lambda_D$) or smallest thicknesses (41–44). In this context, although WO_3 films grown in the range of 373−573 K are promising, the electrical parameters determined for WO_3 films with grain sizes varying in the range of 9−50 nm could provide a database to design a sensor with enhanced performance.

4. SUMMARY AND CONCLUSION

Temperature-dependent dc electrical conductivity of the amorphous and nanocrystalline WO_3 films exhibits the exponential behavior which indicates the semiconducting nature of all the films. Lower conductivity of WO_3 films RT is attributed to their amorphous nature. The conductivity value was found to increase with increasing substrate temperature because of the increasing crystalline nature and preferred orientation of the nanocrystalline WO_3 films along (00 L). The mechanisms of electrical conduction at different temperature regions in all the films are explained in terms of a polaron model and a variable-range hopping model. The conductivity data of WO_3 films were successfully analyzed by the nonadiabatic small polaron hopping conduction theory at higher temperature (180−300 K). It has been found that the conduction mechanism at the temperature range of 120−180 K is due to variable range hopping mechanism. The density of localized states at the Fermi level, $N(E_F)$, has been calculated and it was found to be $\sim 1 \times 10^{19}$ eV^{-1} cm^{-3} for all the films.

Acknowledgment. This material is based on work supported by the Department of Energy under Award DE-PS26-08NT00198-00.

REFERENCES AND NOTES

(1) Meixner, H.; Lampe, U. *Sens. Actuators B* **1996**, *33*, 198–202.
(2) Williams, D. E. *Sens. Actuators B* **1999**, *57*, 1–16.
(3) Wang, X.; Miura, N.; Yamazoe, N. *Sens. Actuators B* **2000**, *66*, 74–79.
(4) Lee, D. S.; Han, S. D.; Lee, D. D. *Sens. Actuators B* **1999**, *60*, 57–63.
(5) Baeck, S. H.; Jaramillo, T.; Stucky, G. D.; McFarland, E. W. *Nano Lett.* **2002**, *2*, 831–834.
(6) Lee, D. S.; Nam, K. H.; Lee, D. D. *Thin Solid Films* **2000**, *375*, 142–147.
(7) Wang, L.; Teleki, S. E.; Pratsinis, S. E.; Gouma, P. I. *Chem. Mater.* **2008**, *20*, 4794–4796.
(8) Kawasaki, H.; Namba, J.; Iwatsuji, K.; Suda, Y.; Wada, K.; Ebihara, K.; Ohshima, T. *Appl. Surf. Sci.* **2002**, *8065*, 1–5.
(9) Ionescu, R.; Llobet, E.; Brezmes, J.; Vilanova, X.; Correig, X. *Sens. Actuators B* **2003**, *95*, 177–182.
(10) Gillet, M.; Delamare, R.; Gillet, E. *Eur. Phys. J. D* **2007**, *43*, 295–298.
(11) Gao, B.; Ma, Y.; Cao, Y.; Yang, W.; Yao, J. *J. Phys. Chem. B* **2006**, *110*, 14391–14397.
(12) Santato, C.; Ulmann, M.; Augustynski, J. *J. Phys. Chem. B* **2001**, *105*, 936.
(13) Deb, S. K. *Sol. Energy Mater. Sol. Cells* **2008**, *92*, 245–250.
(14) Huda, M. N.; Yan, Y.; Moon, C.-H.; Wei, S.-H.; Al-Jassim, M. M. *Phys. Rev. B* **2008**, *77*, 195102–195105.
(15) Shaltout, I. I.; Tang, Y. I.; Braunstein, R.; Shaisha, E. E. *J. Phys. Chem. Solid* **1996**, *57*, 1223–1224.
(16) Sahle, W.; Nygren, M. *J. Solid State Chem.* **1983**, *48*, 154–160.
(17) Berak, J. M.; Sienko, M. J. *J. Solid State Chem.* **1970**, *2*, 109–133.
(18) Salje, E.; Viswanathan, K. *Acta Crystallogr., Sect. A* **1975**, *31*, 356–359.
(19) Lassner, E.; Wolf-Dieter, S. *Tungsten: Properties, Chemistry, Technology of the Element, Alloys, and Chemical Compounds*; Kluwer Academic: New York, 1999.
(20) Ayyappan, S.; Rangavittal, N. *Bull. Mater. Sci.* **1997**, *20*, 103–109.
(21) Georg, A.; Graf, W.; Wittwer, J. *Sol. Energy Mater. Sol. Cells* **1998**, *51*, 353–370.
(22) Wang, X. G.; Jiang, Y. S.; Yang, N. H.; Yuan, L.; Pang, S. J. *Appl. Surf. Sci.* **1999**, *143*, 135–141.
(23) Akl, A. A.; Kamal, H.; Abdel-Hady, K. *Physica B* **2003**, *325*, 65–75.
(24) De Wijs, G. A.; de Boer, P. K.; de Groot, R. A.; Kresse, G. *Phys. Rev. B* **1999**, *59*, 2684–2693.
(25) Methfessel, M.; Paxton, A. T. *Phys. Rev. B* **1989**, *40*, 3616–3621.
(26) The Scherrer equation is $d_{hkl} = 0.9\lambda/\beta\cos\theta$, where d is the size, λ is the wavelength of the filament used in the XRD machine, β is the width of a peak at half of its intensity, and θ is the angle of the peak.
(27) Gullapalli, S. K.; Vemuri, R. S.; Ramana, C. V. *Appl. Phys. Lett.* **2010**, *96*, 171903–171905.
(28) Stankov, N. E.; Atanasov, P. A.; Stanimirova, T. J.; Dikovska, A. Og.; Eason, R. W. *Appl. Surf. Sci.* **2005**, *247*, 401–405.
(29) Bakonyi, I.; Toth-Kadar, E.; Tarnoczi, T.; Varga, L.; Cziraki, A.; Gerocs, I.; Fogarassy, B. *Nanostruct. Mater.* **1993**, *3*, 155–158.
(30) Wu, L.; Tien-Shou, W.; Chung-Chuang, W. *J. Phys. D: Appl. Phys.* **1980**, *13*, 259–266.
(31) Ramana, C. V.; Smith, R. J.; Julien, C. M. *J. Vac. Sci. Technol., A* **2004**, *22*, 2453–2458.
(32) Ramana, C. V.; Julien, C. M. *Chem. Phys. Lett.* **2006**, *428*, 114–118.
(33) Ambily, S.; Menon, C. S. *Thin Solid Film* **1999**, *347*, 284–289.
(34) Mott, N. F.; Davis, E. A. *Electronic Processes in Non-Crystalline Materials*, 2nd ed.; Clarendon: Oxford, U.K., 1979.
(35) Landau, D. *Phys. Z. Sowjetunion* **1933**, *3*, 644–654.
(36) Ajai Gupta, K.; Kumar, V.; Khare, N. *Solid State Sci.* **2007**, *9*, 817–823.
(37) Mott, N. F. *J. Non-Cryst. Solid* **1968**, *1*, 1–10.
(38) Yildiz, A.; Lisesivdin, S. B.; Kasap, M.; Mardare, D. *Physica B* **2009**, *404*, 1423–1426.
(39) Hutchins, M. G.; Abu-Alkhair, O.; El-Nahass, M. M.; Abdel Hady, K. *J. Phys.: Condens. Matter* **2006**, *18*, 9987–9997.
(40) Ogawa, H.; Nishikawa, M.; Abe, A. *J. Appl. Phys.* **1982**, *53*, 44484455.
(41) Du, X.; George, S. M. *Sens. Actuators B* **2008**, *135*, 152–160.
(42) Jin, Z. H.; Zhou, H. J.; Jin, Z. L.; Savinell, R. F.; Liu, C. C. *Sens. Actuators B* **1998**, *52*, 188–194.
(43) Shieh, J.; Feng, H. M.; Hon, M. H.; Juang, H. Y. *Sens. Actuators B* **2002**, *86*, 75–80.
(44) Xu, C.; Tamaki, J.; Miura, N.; Yamazoe, N. *Sens. Actuators B* **1991**, *3*, 147–155.

AM1004514